Sawtooth oscillations in shaped plasmas[a)]

E. A. Lazarus,[1,b)] T. C. Luce,[2] M. E. Austin,[3] D. P. Brennan,[4] K. H. Burrell,[2] M. S. Chu,[2] J. R. Ferron,[2] A. W. Hyatt,[2] R. J. Jayakumar,[5] L. L. Lao,[2] J. Lohr,[2] M. A. Makowski,[5] T. H. Osborne,[2] C. C. Petty,[2] P. A. Politzer,[2] R. Prater,[2] T. L. Rhodes,[6] J. T. Scoville,[2] W. M. Solomon,[7] E. J. Strait,[2] A. D. Turnbull,[2] F. L. Waelbroeck,[3] and C. Zhang[8]
[1]*Oak Ridge National Laboratory, Oak Ridge, Tennessee 37831*
[2]*General Atomics, P.O. Box 85608, San Diego, California 92186-5608*
[3]*University of Texas, Austin, Texas 78712*
[4]*University of Tulsa, Tulsa, Oklahoma 74104*
[5]*Lawrence Livermore National Laboratory, Livermore, California 94550*
[6]*University of California-Los Angeles, Los Angeles, California 90095*
[7]*Princeton Plasma Physics Laboratory, Princeton, New Jersey 08540*
[8]*Academia Sinica, Institute of Plasma Physics, Hefei, China*

(Received 2 November 2006; accepted 21 December 2006; published online 21 March 2007)

The role of interchange and internal kink modes in the sawtooth oscillations is explored by comparing bean- and oval-shaped plasmas. The $n=1$ instability that results in the collapse of the sawtooth has been identified as a quasi-interchange in the oval cases and the internal kink in the bean shape. The ion and electron temperature profiles are followed in detail through the sawtooth ramp. It is found that electron energy transport rates are very high in the oval and quite low in the bean shape. Ion energy confinement in the oval is excellent and the sawtooth amplitude ($\delta T/T$) in the ion temperature is much larger than that of the electrons. The sawtooth amplitudes for ions and electrons are comparable in the bean shape. The measured q profiles in the bean and oval shapes are found to be consistent with neoclassical current diffusion of the toroidal current, and the observed differences in q largely result from the severe differences in electron energy transport. For both shapes the collapse flattens the q profile and after the collapse return to $q_0 \gtrsim 1$. Recent results on intermediate shapes are reported. These shapes show that the electron energy transport improves gradually as the plasma triangularity is increased. © *2007 American Institute of Physics*.
[DOI: 10.1063/1.2436849]

I. INTRODUCTION

The sawtooth instability appears as a regular, periodic reorganization of the plasma core. In the sawtooth ramp, temperature increases in an approximately linear fashion. This is followed by a rapid collapse wherein the core plasma dumps energy into the surrounding region. The increase in central temperature then starts anew. The collapse is due to an instability with poloidal and toroidal mode numbers, m and n of 1, and is associated with having a $q=1$ surface in the plasma. Sawtooth oscillations have defied a first-principles description[1] since their discovery[2] three decades ago.

We attempt here to distinguish the roles of interchange and internal kink stability in the sawtooth collapse. This is accomplished by changing the plasma shape. We find significant differences in both the evolution within a sawtooth period and in the nature of the sawtooth collapse itself. In this paper, interchange, whether ideal or resistive, is taken to mean the *local* instability. The sawtooth instability (toroidal mode number $n=1$) has two types of eigenfunction: the internal kink, originally described by Kadomtsev,[3] and the quasi-interchange described by Wesson,[4] the former becoming unstable when $q<1$ but the latter can be unstable while $q \gtrsim 1$.

In an oval-shaped plasma with simple monotonic pressure and q profiles, the Mercier criterion[5] will be violated while q_0 is somewhat above 1. The destabilizing terms are elongation, κ, and beta poloidal, β_P, whereas triangularity, δ, is stabilizing. Thus, if we make a low-κ bean shape using similar profiles, the Mercier criterion (D_I) can be satisfied with q_0 somewhat below 1. For finite β, the stability criterion for the internal kink remains $q=1$ in both cases. In a circular plasma, the criteria are degenerate and $q=1$ is the marginal point for both the interchange and $n=1$ instabilities. The Mercier criterion is the condition for ideal magnetohydrodynamic (MHD) stability to localized perturbations in a toroidal plasma. If this condition is violated, the magnetic field curvature is unfavorable and the plasma is unstable to a pressure gradient. In this paper, we will be concerned with the resistive interchange criterion (D_R),[6] where the effects of diffusion of the magnetic field are included. This change from the ideal to resistive interchange largely eliminates the stabilization of magnetic shear through field line bending, by allowing the field lines to break. The relationship between the criteria is $D_R=D_I+(H-1/2)^2$, where H (defined in Ref. 6) remains small compared to $\frac{1}{2}$ in our experiments. The resistive interchange criterion can be deconstructed[7] into terms associated with curvature of the magnetic field (or magnetic well), magnetic shear, and pressure gradient. In these experiments, the shear and pressure gradient terms are negligibly small compared to the magnetic well term. By comparing

[a)]Paper VI2 4, Bull. Am. Phys. Soc. **51**, 290 (2006).
[b)]Invited speaker.

 © 2007 American Institute of Physics

Downloaded 12 Aug 2009 to 128.83.61.90. Redistribution subject to AIP license or copyright; see http://pop.aip.org/pop/copyright.jsp

sawteeth in the oval and bean shapes, we should be able to gain insight into the nature of the sawtooth collapse and how it is affected by interchange stability. What was not anticipated was that the changes in plasma shape would result in very large changes in electron and ion transport rates, and these are oppositely directed.

We have previously reported[8] briefly on these experiments. Our purpose here is to present more fully the experimental results and analysis as well as to present new results on shapes intermediate between the bean and oval. This paper is organized as follows. In Sec. II, we discuss the design and operation of the experiment along with a brief characterization of the sawteeth. Section III presents the observed phenomenology in detail, including the dynamics of the sawtooth evolution, the evolution of the ion and electron temperature profiles, the evolution of the q profile, and the response to central electron heating. Recent results on intermediate shapes are also presented. In Sec. IV, we discuss the transport and stability analysis, and our conclusions are presented in Sec. V.

II. EXPERIMENTAL CONFIGURATION

We began our design with a number of constraints in mind for the experiment. We need plasma shapes and conditions consistent with the DIII–D coil currents and the available poloidal field power supplies. Additionally, we required configurations that are created with the same poloidal field circuit, that is, we are not willing to interrupt the experiment and reconfigure the power supplies in order to change the plasma shape. This translates to an ability to alternate plasma shapes on a shot-by-shot basis with high reproducibility. The effects of systematic errors in the diagnostics are minimized by avoiding comparisons of plasmas from different operating periods. The poloidal coils with the solid fill in Fig. 1 are the only ones used in making the oval shape while all the coils and power supplies are used in making the bean shape. To make the oval, we merely need to turn off some power supplies and switch to a different set of control algorithms. Additionally, we desire L-mode plasmas. We desire low β_p to minimize the effect of the pressure gradient on the internal flux surface shape (Shafranov shift). However, the measurements require neutral beam power of 2.5 MW, and thus the poorer confinement of the L-mode is advantageous. Also, an H-mode has steep edge gradients in both plasma pressure and plasma current, requiring a higher-order polynomial in the equilibrium reconstruction simply to allow these edge gradients. The remaining constraints are primarily related to measurement quality, so we take this opportunity to show key diagnostics in Fig. 1. In this figure, we show the boundary shape and the typical plasma shapes at the sawtooth inversion radius. The density is kept low $[n_e(0) \approx 5 \times 10^{19}\ \mathrm{m}^{-3}]$ for several reasons. First, we want good penetration of the neutral beam for a good signal-to-noise ratio for the motional Stark effect (MSE)[9] measurement. Second, electron cyclotron emission cutoff must be avoided. Third, at higher density it is more difficult to avoid a transition to H-mode in the bean shape. Lastly, the toroidal magnetic field, B_T, is chosen to correspond either to center the range of

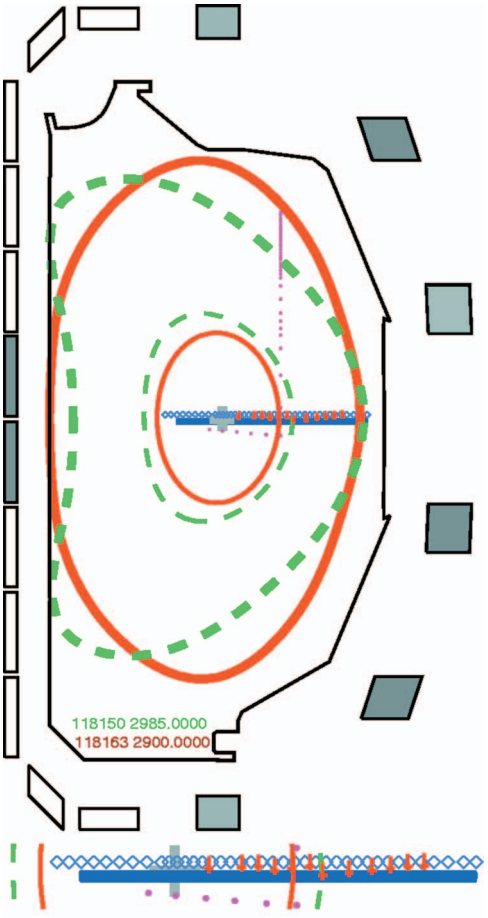

FIG. 1. (Color) Boundary shapes and diagnostic locations for bean and oval. The interior flux surfaces (red for oval and green for bean) are typical positions of the sawtooth inversion radii. The poloidal coils with the solid fill are the only ones needed for making the oval shape. The magenta solid circles are the locations for Thomson scattering (n_e, T_e). The inverted red daggers are the CER (T_i) locations. The cyan diamond shapes are the typical ECE (T_e) locations and the solid blue bar is the range of the MSE (B_θ/B_t) locations. The large gray + is the magnetic axis for both. An expanded view of the midplane diagnostics is shown below the main figure.

the electron cyclotron emission (ECE)[10] radiometer (87–133 GHz) on the plasma center or to position electron cyclotron heating (ECH) deposition (110 GHz) near the magnetic axis.

The reader might look at the shape of the surfaces at the inversion radius in Fig. 1 and question whether the shapes in the core are sufficiently different to observe differences in the interchange properties. An axial expansion of $V^{\dagger\dagger}$ from Eq. (26) of Ref. 7 offers a good indication; $V^{\dagger\dagger} < 0$ being required for stability,

$$V^{\dagger\dagger} = \frac{1}{2\pi^2 R_0^3}\frac{\kappa^2+1}{2\kappa}\left[\frac{1}{q^2} - \frac{2}{\kappa^2+1} + \frac{2(\kappa-1)}{\kappa^2(\kappa+1)}\beta_p - \frac{\kappa^2-1}{\kappa^2+1}\frac{R_0}{R_T}\right], \tag{1}$$

where $V^{\dagger\dagger} \propto D_R$, the resistive interchange criterion. As κ is increased, the ratio of the curvature of the line of tip radii, R_T, must increase to prevent the overall factor from decreasing. One can see by inspection that for $q \sim 1$ and $\beta_p \sim 0$,

Downloaded 12 Aug 2009 to 128.83.61.90. Redistribution subject to AIP license or copyright; see http://pop.aip.org/pop/copyright.jsp

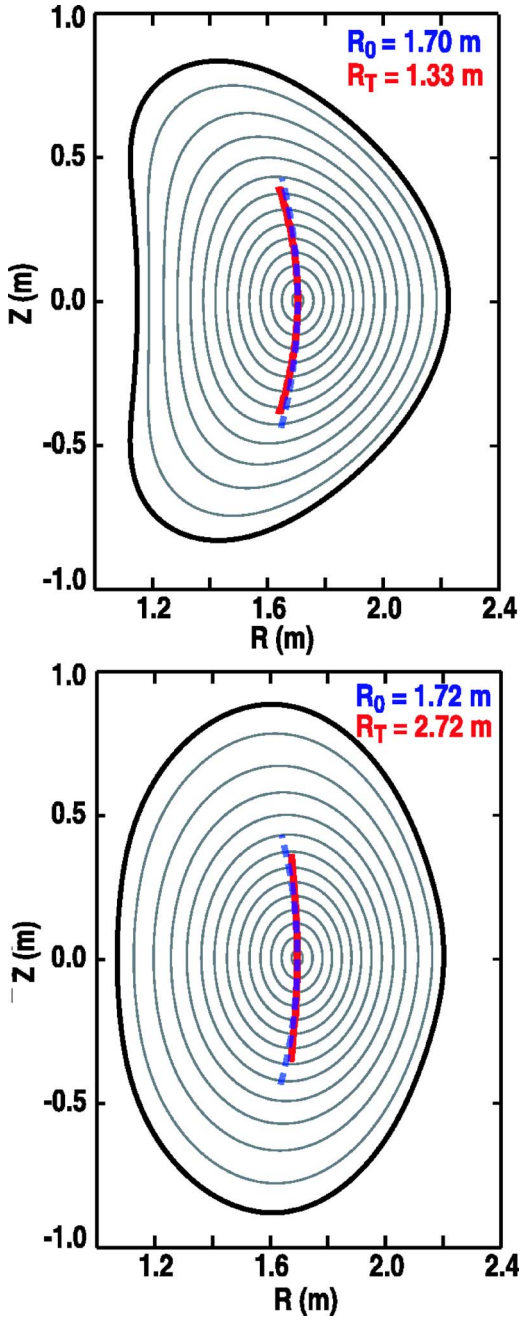

FIG. 2. (Color online) A comparison of the curvature of the line of tip radii, R_T, to the axial major radius. R_0 for bean and oval plasmas. The solid line is constructed on ~100 surfaces where $q<1.1$. The dashed line is a circle of radius R_0.

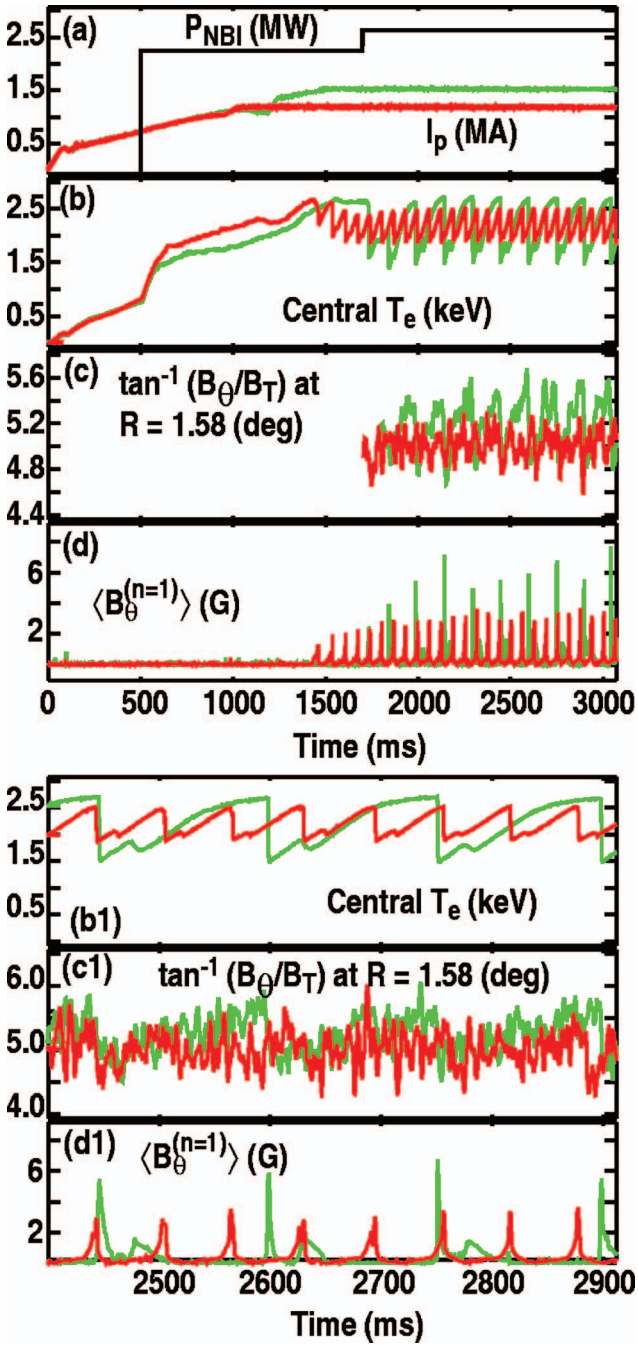

FIG. 3. (Color) Discharge evolution time evolution of selected quantities from $t=0$ to 3000 ms. (Green is the bean shape and red is the oval.) (a) Plasma current and neutral beam heating (NBI) power. (b) Central T_e from the ECE measurement. (c) Central pitch angle, γ_P, from the MSE measurement. (d) $\langle \delta B_\theta^{n=1} \rangle$ at the vessel wall on the outside midplane. (b1), (c1), and (d1) are expanded in time for greater detail. (c) is smoothed for clarity and to show the correlation of γ_P with the sawtooth cycle; (c1) is not smoothed.

$R_0/R_T=1$ is the marginal stability position. R_T and R_0 are shown in Fig. 2, and we see that in the oval $R_0/R_T=0.6$ while in the bean $R_0/R_T=1.3$. Thus, one might expect to see substantial differences as reported here. Equivalent axial expressions that exhibit explicitly the effect of triangularity may be found in Ref. 11, however they are more difficult to evaluate accurately from experimental equilibrium reconstructions because a complete description of each surface in a particular analytic form is required.

This experiment, comparing sawtooth behavior in bean and oval shaped plasmas, has been carried out over a number of years. The results are highly reproducible. The primary changes have been improvements in diagnostics that have provided better insight into sawtooth dynamics. The differences in sawtooth behavior resulting from the plasma shaping overwhelm any possible differences in tokamak wall conditions. The sawtooth period is unchanged from one collapse to the next for a single discharge or for repeated shots. Typical time histories are presented in Fig. 3. As the plasma current is ramped, neutral beam injection (NBI) is started at 500 ms. We anticipated some problems with locked modes in

Downloaded 12 Aug 2009 to 128.83.61.90. Redistribution subject to AIP license or copyright; see http://pop.aip.org/pop/copyright.jsp

the oval, and this early beam is intended to avoid any such issues. At 1700 ms, that beam is turned off and the beam viewed by MSE and central charge exchange recombination (CER)[12] diagnostics is turned on. This beam remains on continuously for 3 s, and data are collected between 2500 and 4500 ms.

Before 2500 ms, the current profile has fully relaxed, as evidenced by a constancy of the pitch angle, $\gamma_P \equiv \tan^{-1}(B_\theta/B_T)$, aside from perturbations related to the sawtooth on all the chords viewing the central region of the plasma. The central T_e traces in Fig. 3(b) show typical behavior; the sawtooth amplitude and period are larger in the bean than the oval. (The sawtooth amplitude will be defined as $[T_e(t_c^-)-T_e(t_c^+)]/T_e(t_c^+)$, where t_c is the time of occurrence of the collapse.) The pitch angle, Fig. 3(c), shown smoothed here, shows greater modulation depth and an abrupt change at the sawtooth collapse in the bean but less modulation depth and no obvious change at the sawtooth collapse in the oval. The perturbation in the $n=1$ component of B_θ at the outside midplane, Fig. 3(d), also shows different characteristics. For the oval $\langle \delta B_\theta^{n=1} \rangle$ rises during the sawtooth ramp due to precursor oscillations. For the bean there are no precursor oscillations and $\langle \delta B_\theta^{n=1} \rangle$ spikes to a larger amplitude at the time of the sawtooth collapse.

In Ohmic plasma ($T_i \ll T_e$) the sawtooth periods, τ_S, are typically 54 ms in the bean and 20 ms in the oval plasmas, about half the values of τ_S found in these experiments with low power NBI, where $T_i \gtrsim T_e$ and fast ions contribute 1/4 to 1/3 of the total stored energy. In the experiments described here, approximately half the neutral beam power is absorbed by the electrons.

III. EXPERIMENTAL RESULTS

In this section, we present a detailed report of the experimental results. Much of our understanding of the sawtooth behavior has resulted from creating movies of T_e profiles from ECE with a 5 or 10 μs resolution. An examination of the response to a brief pulse of ECH has been particularly illuminating. We cannot show movies here but we will describe some of them in reporting on this experiment. We begin this section with a table of representative quantities of interest for four plasmas (Table I); bean and oval shapes at two values of plasma current. These cases (B1, B2, O1, and O2) will be described in greater detail later in this section. The larger I_p values are the limits of the experiment. In the bean, those limits are due to the coil current limits, while in the oval it is this configuration of the power supplies chosen to allow alternating shapes on successive shots that limits the plasma current.

A. A phenomenological description of sawtooth collapse

When operating the experiment, the first prominent distinction in the sawtooth behavior between the two shapes is the difference in the character of the sawtooth cycle (Fig. 4). Within a sawtooth cycle, there are generally oscillations of much higher frequency than $1/\tau_S$, typically several kHz, associated with the $m/n=1/1$ instability itself. Those occurring prior to the collapse are called precursor oscillations and those following the collapse are called successor oscillations. The oval has large precursor oscillations and minimal successor oscillations. The bean has no detectable precursor oscillation but larger successor oscillations than the oval. The bean also has a larger sawtooth amplitude and longer period than the oval. Both show an event we refer to as a relaxation event (RE) at about 25% of the sawtooth period where the reheat stops and then begins again. We avoid calling this a partial reconnection as we see no evidence of reconnection.

TABLE I. Typical values: I_p is plasma current, B_T is applied toroidal field, V is plasma volume, $\bar{n}_e$ is line-averaged density, ℓ_i is plasma inductivity, W_{MHD} is plasma stored energy inferred from the applied vertical field, τ_S is the sawtooth period, q_{95} is the safety factor at 95% of the normalized poloidal flux, τ_E^{th} is the energy confinement time of the thermal plasma (neglecting fast ions), $\tau_E^* \equiv$(total stored energy/total input power), $\beta_{p1} \equiv [\bar{p}_1 - p(r_1)]/(2\mu_0 B_{\theta_1})$, where "1" refers to the location of $q=1$, it is the "Bussac beta" (Ref. 13), and $\delta T_e(0)$ is the drop in central electron temperature at the sawtooth collapse.

Case	B1	B2	O1	O2
Shape	Bean	Bean	Oval	Oval
Shot no.	113920	118162	113915	118164
I_P (MA)	1.38	1.52	0.88	1.18
B_T (T)	1.79	1.85	1.80	1.85
V (m^3)	17.5	17.6	20.1	20.1
$\bar{n}_e(\times 10^{19}$ $m^{-3})$	2.0	2.5	1.9	2.75
β_P	0.22	0.24	0.45	0.38
ℓ_i	1.24	1.15	1.41	1.29
W_{MHD} (MJ)	0.25	0.34	0.24	0.37
τ_E^* (ms)	93	127	90	140
τ_S (ms)	90	154	59	80
q_{95}	3.9	3.6	5.4	4.2
τ_E^{th} (ms)	–	75	–	75
β_{p1}^b	–	0.2	–	0.2
Max $[T_e(0)$ (keV)]	2.8	2.7	2.7	2.5
$\delta T_e(0)$ (keV)	1.2	1.3	0.6	0.6

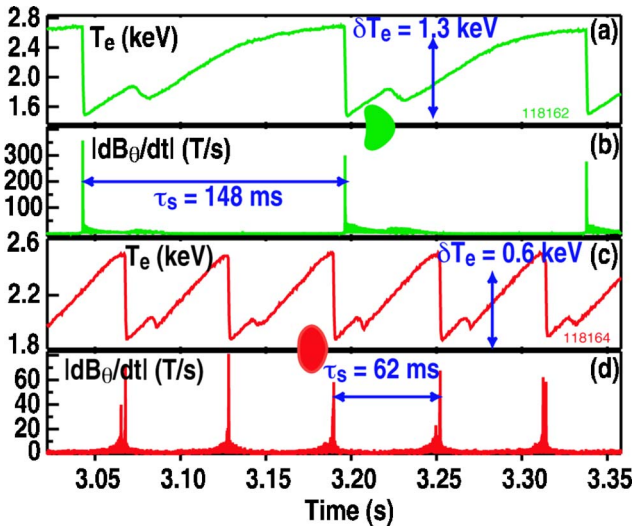

FIG. 4. (Color online) Sawteeth in bean and oval plasmas: (a) and (c) Central T_e vs time. (b) and (d) $|\dot{B}_\theta|$ vs time.

Downloaded 12 Aug 2009 to 128.83.61.90. Redistribution subject to AIP license or copyright; see http://pop.aip.org/pop/copyright.jsp

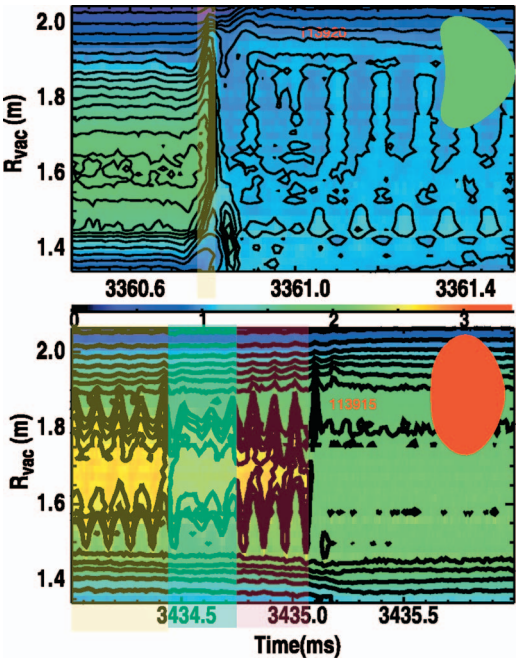

FIG. 5. (Color) Contour map of the electron temperature across a sawtooth collapse in bean and oval plasmas; space vs time. The color bar between the panels ranges from 0 to 3 keV. R_{vac}, as defined in the text, can be several cm in error relative to $R(\psi)$, radii corresponding to equal flux spacing. The collapse event in the bean is the shaded region. The four phases in the oval, as described in the text, are separated by the shading.

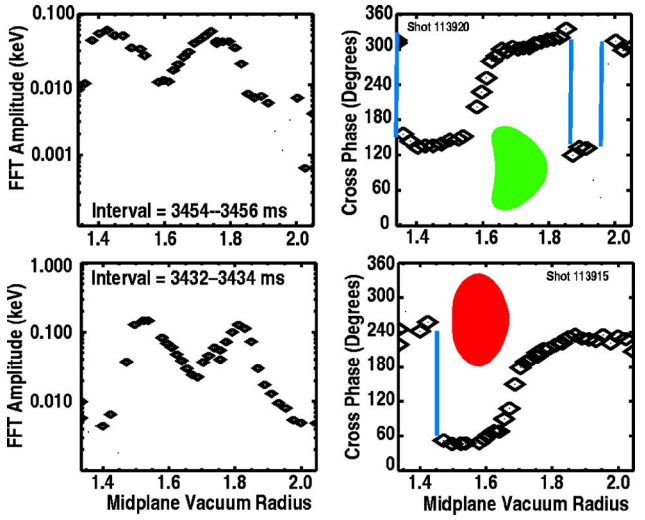

FIG. 6. (Color online) δT_e, fluctuation amplitude and phase shifts from the cross-correlation of the ECE channels with a signal from external magnetic probes at the $n=1$ frequency.

In the oval, we cannot see evidence of why this relaxation occurs. In the bean, a burst of $n=1$ activity can be seen on the magnetic probes at the time of the relaxation event [Fig. 4(b)].

We focus next on the electron temperature behavior across the sawtooth collapse (Fig. 5). In the presentation of ECE data, we will often use R_{vac} rather than use ECE frequency as a radial coordinate. $R_{\mathrm{vac}} \sim R_0 * B_{T0}(0)/2\omega_{ce}$, where B_{T0} is the toroidal field in the absence of plasma. The cyclotron frequencies correspond to the center of the bandwidth selected by the ECE radiometer filters. This gives a reasonable spatial perspective while avoiding the need for an equilibrium calculation to map ECE radiometer frequencies to a spatial variable. The upper panel of the color map shows the bean as the sawtooth collapses. Essentially, there is no core activity in the bean prior to the collapse and the hot core makes an excursion to the outboard side in about 40 μs at 3360.7 ms. After the collapse, a double island structure is seen in the collapsed core.

The oval shown in the lower panel exhibits a growing precursor oscillation more commonly seen with a sawtooth cycle. Prior to the last four oscillations, there is evidence of a beating of this primary mode with a second mode. This second mode is a fishbone oscillation.[14] There are several fishbone bursts within each sawtooth cycle, each lasting a few milliseconds and each sweeping down in frequency during the burst. Finally, one of the bursts sweeps down to the primary frequency and beats against it. After that, the oscillation is more severe as evidenced by the modulation depth and only a few cycles remain before collapse. If we define the collapse time in a way that is analogous to the bean, the departure of the hot spot from the core, that time is about 70 μs.

We turn to the analysis of the T_e fluctuations, which are interesting in their own right and also pave the way for the analysis of the q profile. We calculate the cross correlation of the ECE signals with the $n=1$ component of dB_θ/dt obtained by differencing two outer midplane magnetic probes. From this we get the relative phase of the radial ECE channels along with the coherence of the channels to the magnetic perturbation (Fig. 6). In the upper panel, we display the analysis results for a bean in a 2 ms window after the collapse. Prior to the collapse, there is no coherence between the ECE and the magnetic probe measurements, consistent with the lack of a visible precursor. In the post-crash phase, there is a phase shift of 180 degrees such as the jump at $R=1.86$ m, which matches a shift of opposite sense on the inboard side ($R=1.34$ m) indicating an island, consistent with the contours seen in Fig. 5(a). (We assume that the jump at $R=1.96$ m also has a corresponding jump on the inboard side, beyond our viewing range.) The lower panel shows the cross-correlation analysis in an oval, in a 2 ms interval during the precursor oscillation but before the beating against the fishbone described above. Here we see a phase jump on the inboard side, but no corresponding jump on the outboard side.

We demonstrate with a simple model that the existence of this single phase jump on the high-field side distinguishes an ideal quasi-interchange (QI)[4] from a resistive internal kink (RIK).[3] In our simple model, the eigenfunction has only $m=1$ and 2 components called ξ_1 and ξ_2, respectively. All that really counts in this model is that the $m=1$ component of the eigenmode not be the rigid displacement characteristic of an $n=1$ internal kink. The eigenfunction will be $\xi(r,\theta,t) = \xi_1(r)\cos(\theta - t) + \xi_2(r)\cos(2\theta - t)$ and the fluctuation signal seen on the ECE radiometer will be $\xi(r,\theta,t)\cdot\partial T_e(r,t)/\partial r$. The components of $\xi(r,\theta,t)$ and an assumed $T_e(r,t)$ are shown in Fig. 7(a). The FFT amplitude and phase are then

Downloaded 12 Aug 2009 to 128.83.61.90. Redistribution subject to AIP license or copyright; see http://pop.aip.org/pop/copyright.jsp

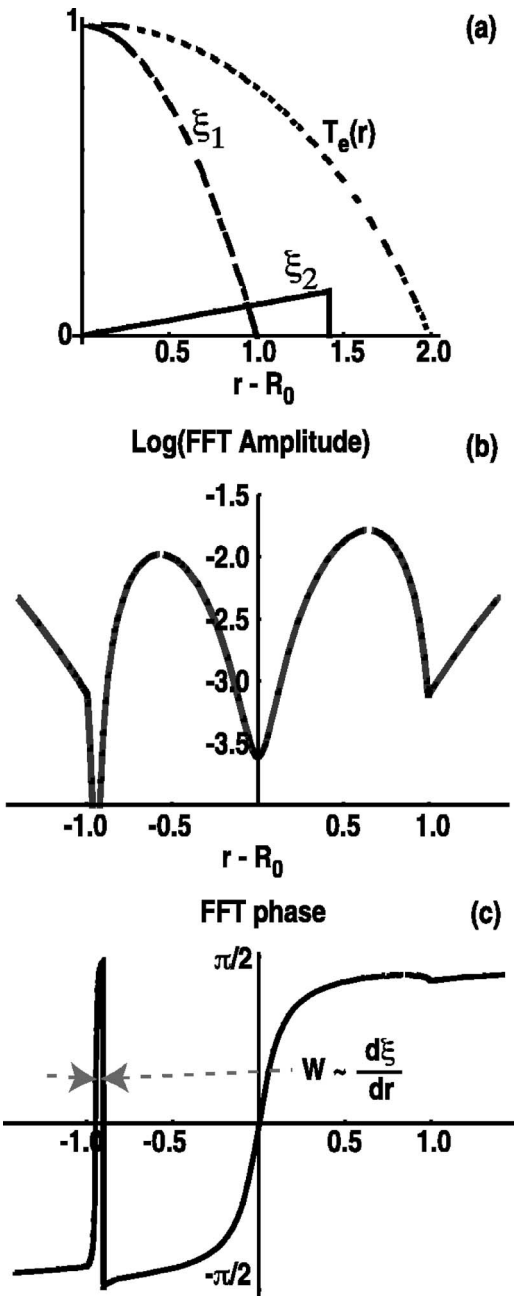

FIG. 7. (a) The components of the assumed eigenfunction for a quasi-interchange, ξ_1 and ξ_2, and T_e profile; (b) δT_e, the fluctuation amplitude, which does not return to zero at the center because the T_e profile is measured slightly below the plasma center, and (c) phase shifts from the cross-correlation of the ECE channels with an external magnetic probe at the $n=1$ frequency. The width W is proportional to the inverse of the slope $[d\xi_1/dr]^{-1}$, where ξ_1 intersects ξ_2.

shown in the lower panels. The important feature is the phase jump and return that occur together on the inboard side. The width, W, in the lower panel will depend on the actual shape of the eigenmode as well as the temperature profile, $T_e(r)$. As will be shown in Sec. V, the $m=1$ components from ideal stability calculations do not return to zero as rapidly as our model, so W will be larger. Were there an island, there would also be a jump of opposite sense on the low-field side. If the eigenmode were an internal kink (top hat), the phase jump and the return would precisely overlay each other and thus cancel [$W \rightarrow 0$ in Fig. 7(c)]. This evidence shows that 2 ms before collapse the oval is a QI. The wobble of the axis (precursor oscillation) is ideal behavior with the axis undergoing a helical excursion, otherwise we would see matching inboard and outboard phase jumps, as previously explained. Correlation analysis during the last few cycles after the appearance of the fishbone still shows the single phase jump on the high-field side. We do not believe it to be plausible that in the last 70 μs the structure of the eigenmode would change to a kink, so we conclude the collapse is a quasi-interchange.

The evolution of the T_e profiles differs greatly between bean and oval. In Fig. 8(a), we show a sequence of radial T_e profiles at times relative to the collapse time, t_c, for an oval. Although the helical distortion of the axis becomes quite severe, the correlation analysis does not indicate tearing has occurred. By way of comparison, we show in Fig. 9 the collapse of a bean sawtooth. The first time one could imagine seeing an indication of a perturbation in the T_e profile is 40 μs before the collapse, and 10 μs later the outer half has caved in. Flattening near the axis, as seen in the oval, is not observed. In neither shape do we see any evidence of tearing prior to the collapse. In the bean, after the collapse there is evidence an island is present, so we know the plasma has reconnected. This does not occur prior to the 40 μs interval of the collapse. In the oval, if tearing occurs, it does so during the last cycle of the precursor oscillations.

B. The response to electron heating with centrally deposited ECH

Before turning to the ion behavior, it is helpful to look at the plasma response to about 3/4 MW centrally deposited ECH. The result is shown in Fig. 10(a). We see that the bean shape heats nicely with $T_e(0)$ reaching 3.9 keV, as compared to 2.7 keV for a similar discharge without ECH [Fig. 10(b)]. The sawtooth period, τ_S, is decreased by a few percent. The baseline of the sawteeth without ECH is shown as a dashed line in the figure. With the addition of ECH, this baseline rises by ~0.2 keV. The oval presents a less regular picture with the precursor $m/n=1/1$ oscillation present throughout most of the sawtooth interval. Here the base of the sawteeth rises about 0.6 keV while the peak sawtooth δT_e is little changed, remaining about 0.6 keV. That the amplitude of the sawtooth remains about the same while the base rises is an indication there is little localization of the heating. This is evidence that electron energy confinement in the oval is quite inferior to that in the bean. τ_S becomes irregular with the period longer when partial reconnections are more severe. Looking at sawteeth with minimal partial reconnection [Fig. 10(a) at $t \approx 3770$ ms], the period τ_S is shortened from 58 to 37 ms, much larger than the 5% difference in τ_S for the bean shape.

C. Ion temperature behavior in beans and ovals

In DIII-D with new detectors for the CER diagnostic, the ion temperature profile is followed through a sawtooth cycle for the first time. Central values are compared to T_e for the bean in Fig. 11(a) and the oval in Fig. 11(b).

Downloaded 12 Aug 2009 to 128.83.61.90. Redistribution subject to AIP license or copyright; see http://pop.aip.org/pop/copyright.jsp

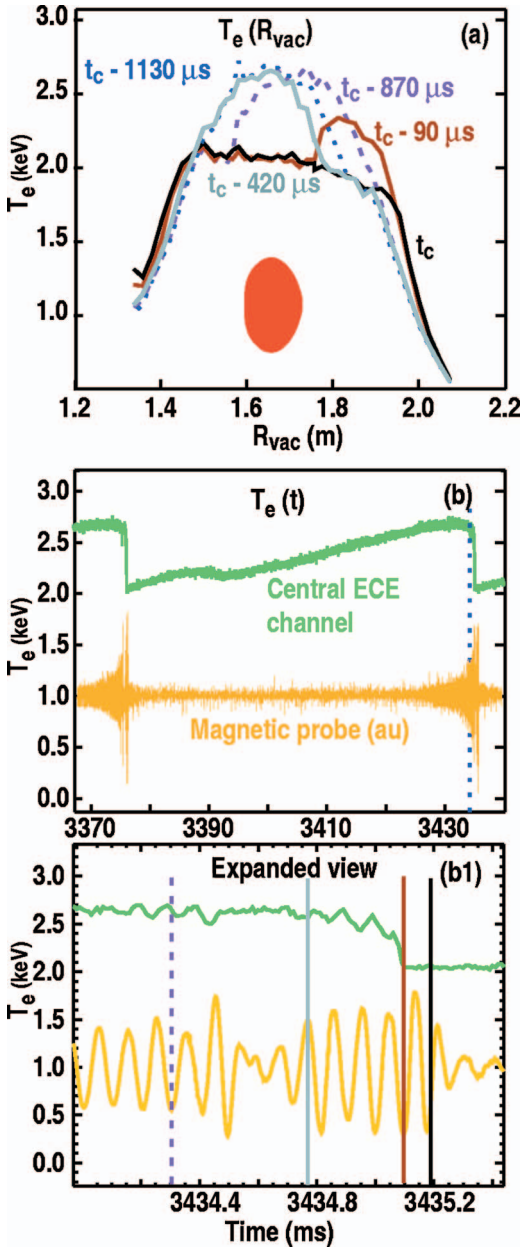

FIG. 8. (Color) The evolution of the radial T_e profiles during the sawtooth collapse in the oval shape. (a) $T_e(R_{vac})$ from ECE at selected times before the collapse time, t_c. (b) Central T_e and $\dot{B}_\theta$ over the sawtooth interval, expanded in (b1). The vertical bars correspond to the profile times in (a).

Until the relaxation event (RE), no central ∇T is developed. This is illustrated with the ion temperature profiles in Fig. 12, where we show the radial profiles at selected times. There are a number of characteristic features to point out in Fig. 11. The most obvious is that the ion sawtooth amplitude is more than twice that of the electrons in the oval shape. In the bean, the RE ends before 2940 ms and after that time we see that $T_i(\rho)$ starts to peak up. In the oval, the RE ends before 2965 ms and then $T_i(\rho)$ starts to peak. The bean characteristically exhibits a "rollover" in T_i at about 2/3 τ_S where T_i begins to decrease while T_e continues to increase. This behavior is not seen in the oval shape. Here, "rollover" is

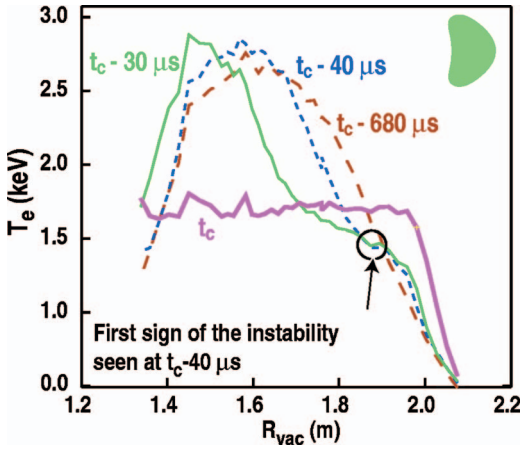

FIG. 9. (Color) The evolution of the radial T_e profiles during the sawtooth collapse in the bean shape.

restricted to exclude the situation in which T_i and T_e decrease together, which does occur in the oval shape when the $m/n = 1/1$ oscillations become large.

D. Equilibrium reconstruction and the safety factor

Accurate equilibrium reconstruction using the EFIT[15] code is critical to successful stability analysis. The difficulty in this problem is that a specification of the plasma pressure requires a calculation of the fast ion component, which in itself requires an equilibrium. The thermal part of the pressure can be obtained directly from the data but is often a poor approximation to the total pressure in the central region. The usual approach is to create an equilibrium using MSE data and external magnetic measurements. The total pressure is computed, in our cases using TRANSP. Now a second equilibrium is calculated where that total pressure is input as data in the least-squares minimization along with the previ-

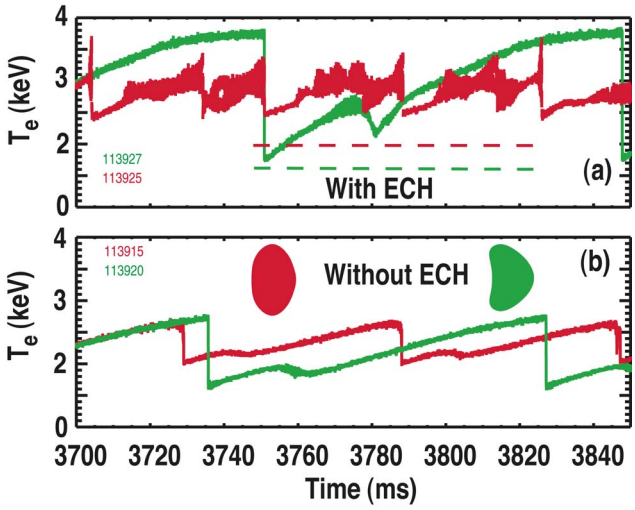

FIG. 10. (Color online) (a) Central T_e when 3/4 MW of central ECH is added. In the upper panel the short dashed lines are the location of the base of the sawtooth *without* ECH. (b) Similar plasmas without ECH.

Downloaded 12 Aug 2009 to 128.83.61.90. Redistribution subject to AIP license or copyright; see http://pop.aip.org/pop/copyright.jsp

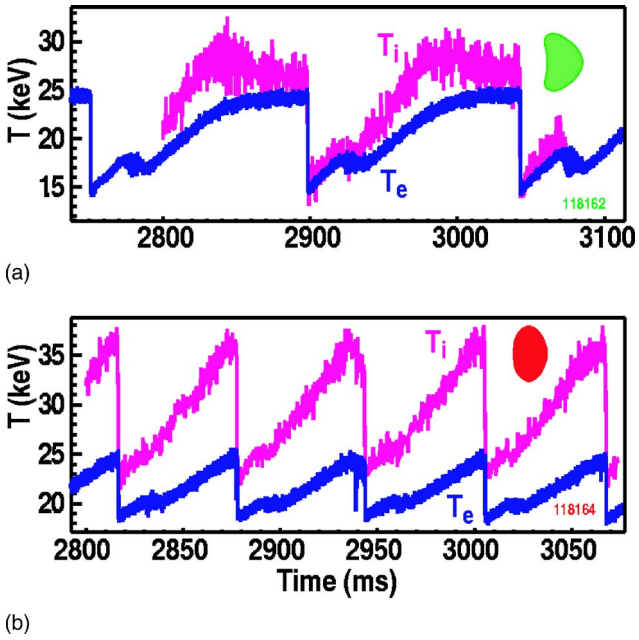

FIG. 11. (Color online) Central T_i and T_e for (a) a bean shape and (b) the oval. The time resolution is 5 μs for T_e and 320 μs for T_i.

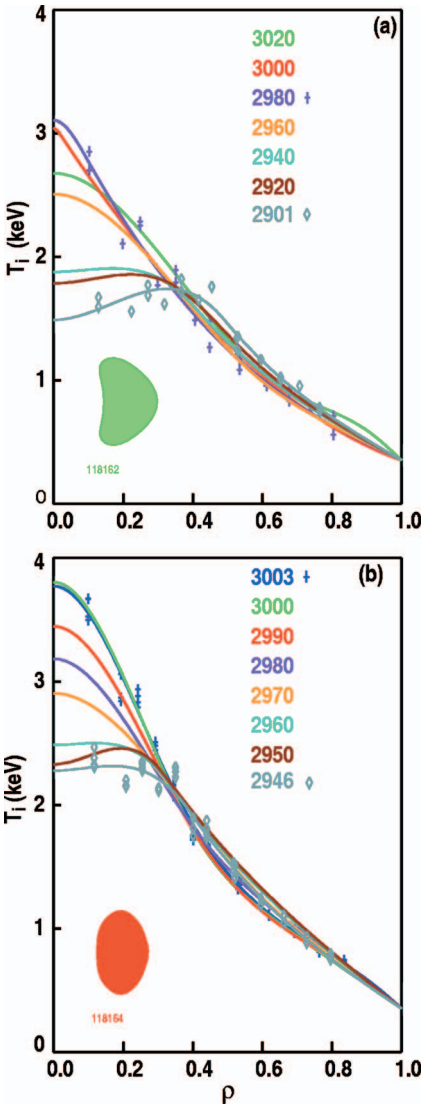

FIG. 12. (Color) Spline fits of $T_i(\rho)$ at selected times in a sawtooth cycle for (a) a bean shape and (b) the oval. At two times, the data used in the fit are displayed. ρ is the square root of the normalized toroidal flux. Times refer to Fig. 11.

ous data. Calculating the total pressure based on one equilibrium solution and using this $p(\psi)$ in a subsequent iteration[16] is often referred to as "kinetic EFIT."

We found two deficiencies in this process. The first was that the final equilibrium did not show T_e from ECE to be a flux surface quantity. That is, ECE did not exhibit reflective symmetry about the magnetic axis. The second deficiency was, in fact, an incorrect assumption on our part that $q_{\min}$ should not be above unity in cases like O1. From cases in the operating years 1999, 2001, and 2003, our best efforts resulted in $q_{\min}$ in the range 1.02–1.06. However, the first deficiency we mentioned is quite serious for this experiment, which relies extensively on ECE and accurate equilibrium information in the axial region. Parenthetically, cases like B1 showed monotonic q profiles with $q_0 < 0.9$ in all operating periods for this experiment.

We believe the procedure used here is superior, in that the magnetic axis is properly located. Within a single equilibrium calculation we use the ECE signals (T_e) as a constraint[17,18] on the flux surface geometry along with the MSE data. This assures a location for R_0 from the equilibrium that is consistent with the central T_e profile. Then the total pressure is calculated in the usual way and added as a fitting constraint in the usual way, as $p(\psi)$ at a number of points equally spaced in ψ from the axis to the boundary. This represents an improved procedure in that we do not prescribe an erroneous $p(\psi)$ based on a previous equilibrium calculation. Rather, we assert that T_e labels a flux surface and adjust the constraint between iterations within a single equilibrium calculation. Of course, this can only be used if ECE signals span a sufficient region of the plasma. Additionally, this is less numerically stable than the usual "kinetic EFIT" and we found it necessary to enforce up/down symmetry to achieve adequate convergence in EFIT. Fortunately, the experiment was designed such that the plasmas are quite symmetric about the midplane. Initially we did this in an oval plasma where the usual kinetic equilibrium reconstruction efforts yielded a result that q did not drop below 1.02 before the sawtooth crash. As discussed in more detail below, the q profile and boundary shape are then used as input to TRANSP where then total pressure, including fast ions, is calculated. This T_e-constrained solution reduced $q_{\min}$ from a value above 1.02 to 1.00; that is, the differences from the traditional approach are not large. The major attraction of this approach to equilibrium reconstruction is that our solution is geometrically correct in the vicinity of the magnetic axis.

The first results we want to present are for cases B1 and O1 of Table I, also shown previously in Figs. 6 and 10(b). The case of the oval is shown in Fig. 13. Total pressure and safety factor are displayed at 13% and 87% of the sawtooth period. The distinctive features are the small change during a sawtooth cycle and the lack of any central shear. While $q_{\min}$

Downloaded 12 Aug 2009 to 128.83.61.90. Redistribution subject to AIP license or copyright; see http://pop.aip.org/pop/copyright.jsp

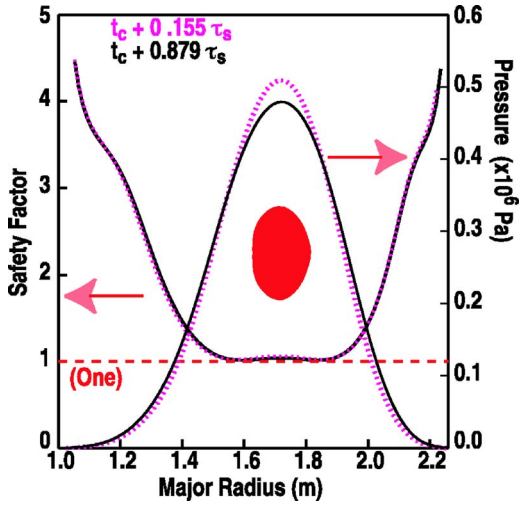

FIG. 13. (Color online) $q(R)$ and $p(R)$ from equilibrium reconstruction with EFIT at two times in the sawtooth cycle for an oval shape. t_c is the collapse time and τ_S is the sawtooth period. Case O1.

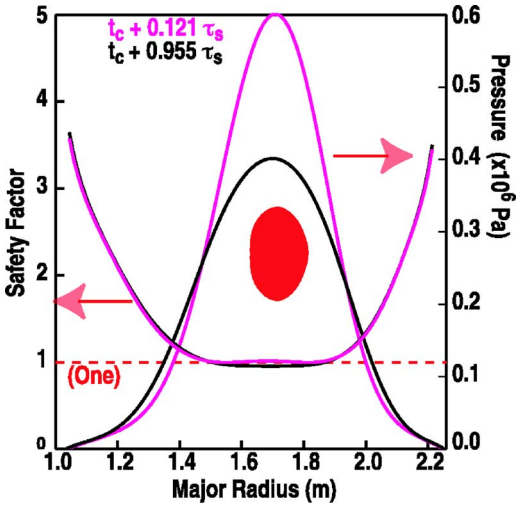

FIG. 15. (Color online) $q(R)$ and $p(R)$ from equilibrium reconstruction with EFIT at two times in the sawtooth cycle for an oval shape. t_c is the collapse time and τ_S is the sawtooth period. Case O2.

remains above unity, this is perhaps just a matter of accuracy, however such profiles have been shown theoretically to be unstable.[19] The behavior of the bean (Fig. 14) is entirely different. The pressure evolution is substantial. This is even seen in the plasma diamagnetism, which shows about 15% of the plasma stored energy is lost from the plasma on each sawtooth collapse. The safety factor evolves into a monotonic profile after the RE and a typical minimum during the sawtooth cycle is $q_0 \lesssim 0.85$.

If we look carefully at the first time in Fig. 14, which is 13 ms after the sawtooth collapse, we find q crosses 1 at $R = 1.47$, 1.55, 1.79, and 1.91. This is in reasonable agreement with the locations of phase jumps in the ECE cross correlation [Fig. 6(b)] taken 2 ms after the collapse. These phase jumps demand a double crossing of $q=1$, indicative of the double island structure. We do not know the details of the evolution of this small island, but we do know it has vanished by the RE that occurs 30 ms after the sawtooth collapse, after which the q profile is again monotonic. This correlation of equilibrium reconstruction, based on MSE measurements of the pitch angle, γ_P, with ECE cross correlation that does not depend at all on the MSE measurements, provides additional confidence in the correctness of our result. Additionally, the raw MSE data shown in Fig. 3(c) suggest a qualitative difference between the two shapes with a more dramatic change in q at the collapse in the bean. (The temporal resolution of the MSE is 0.5 ms.) In the bean shape, one can see the distinct drop in B_θ between time samples at the collapse time. In the oval, one cannot see these distinct changes; as shown in Fig. 3(c), part (c1), B_θ meanders down over 2 or 3 ms and we discern no particular character to this drop. One can resolve in a statistical sense that a decrease in central B_θ occurs near every sawtooth collapse, but one cannot determine exactly when, in contrast to the clear drop detected in the bean.

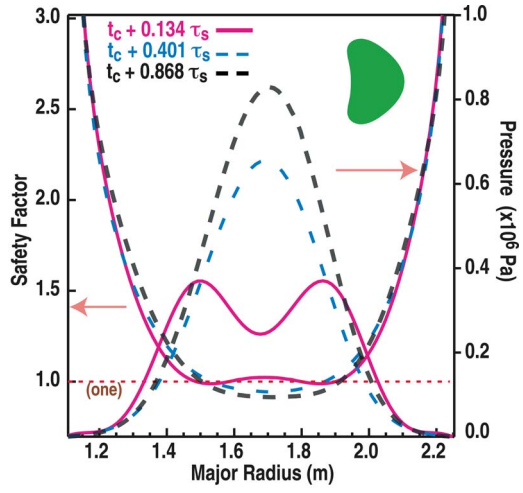

FIG. 14. (Color online) $q(R)$ and $p(R)$ from equilibrium reconstruction with EFIT at three times in the sawtooth cycle for a bean shape. t_c is the collapse time and τ_s is the sawtooth period. Case B1.

Previous reports[20–22] have stated that q_0 remains well below unity after the sawtooth collapse. From the descriptions of very small changes, δq_0 on each sawtooth collapse, these appear to be similar to the type of sawtooth we observe in ovals. However, previous work on DIII-D[9,23] has also reported q_0 returning to unity, as observed in this work.

For the higher current oval case, O2, our reconstruction shows $q_{\min}$ dropping below unity to 0.95 (Fig. 15). The lower current ($I_p = 0.9$ MA) cases are from 2003 and earlier operating years. The higher current ($I_p = 1.25$ MA) cases are from 2004. The MSE hardware and calibration were somewhat different for the two cases, but we do not have a better comparison. Note also that the pressure change is also larger for the case O2 than O1. However, there appears to be no significant change in the gross sawtooth characterization between the lower and higher plasma current cases. In the experiment and analysis, we are confident of differences such as the q profiles in case B1 relative to O1 or B2 relative to O2. We do not have the same level of confidence in comparisons such as O2 to O1 and try to avoid using cases from different operating days in our analysis.

Downloaded 12 Aug 2009 to 128.83.61.90. Redistribution subject to AIP license or copyright; see http://pop.aip.org/pop/copyright.jsp

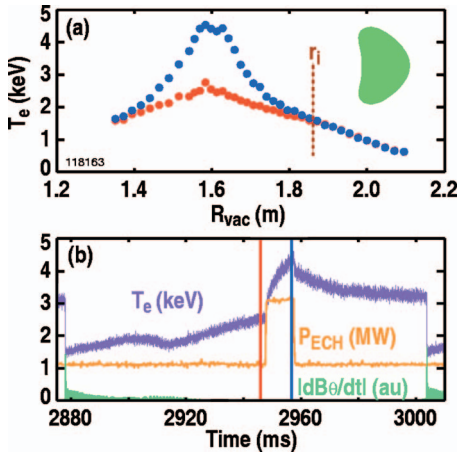

FIG. 16. (Color) (a) $T_e(R_{vac})$ (keV) for two times indicated in (b) at the beginning and end of an ECH pulse in the bean shape. (b) Central T_e for the single sawtooth period along with $|\dot{B}_\theta|$ at the outside midplane normalized to its peak value during the sawtooth cycle, and the ECH heating pulse displaced upward by 1 MW.

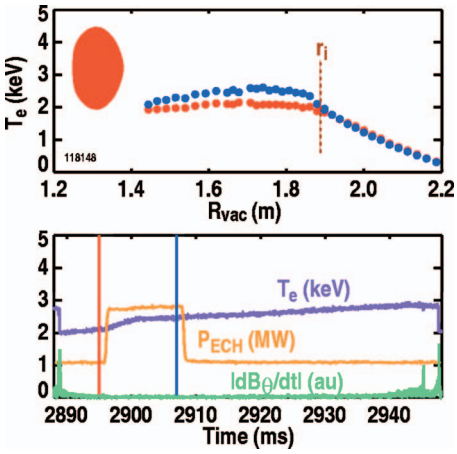

FIG. 17. (Color) $T_e(R_{vac})$ (keV) for the two times indicated in (b), at the beginning and end of an ECH pulse in the oval shape. (b) Central T_e for the single sawtooth period along with $|\dot{B}_\theta|$ at the outside midplane normalized to its peak value during the sawtooth cycle, and the ECH heating pulse displaced upward by 1 MW.

E. The response of T_e to an ECH pulse

Some of the most dramatic results are elucidated by examining the response to a short (10 ms) pulse of ECH aimed near the plasma center ($\rho \approx 0.05$). The most revealing result comes from such heating in the oval shape timed to be after the RE but prior to the growth of the $m/n=1/1$ precursor. Care needs to be taken so the ECH power is not so large as to excite these oscillations. The method here is to heat with ECH in 10 ms pulses with a regular repetition rate that is smaller than the sawtooth rate. Thus the timing of the ECH relative to the sawtooth is random and we search the results for important cases. We begin our discussion with the bean shape, shown in Fig. 16. In the upper panel, the radial profile $T_e(R_{vac})$ is shown just prior to the ECH pulse and again just before terminating the pulse. The ECH deposition is near $\rho = 0.05$. (It varies a bit between gyrotrons.) The lower panel shows timing information; central T_e, $\dot{B}_\theta$, and the ECH power are shown. We note the timing of the ECH pulse is when $\dot{B}_\theta$ is small. ($\dot{B}_\theta$ is virtually all from the $n=1$ Fourier component.) Even before the ECH pulse, a distinct central ∇T_e is visible. Also, the slight hollowness in the center is the result of our choice to heat slightly off axis.

Now we turn to the oval behavior illustrated in Fig. 17. Here there is minimal response to the ECH heating pulse unless the $m/n=1/1$ oscillation is present. There is no sign that a local gradient is being established, in marked contrast to the bean, where one sees the center heating first and the increased ∇T_e spreading outward from the axis. In the oval, the evidence of heating is that the entire central region, to approximately r_i, shows an increased T_e indicating that outside this region an increase in ∇T_e can be sustained. Note that the central power density of the ECH absorbed is more than 10 times the neutral beam power deposited in the electrons. The relationship of the $m=1/n=1$ MHD activity to the localization of heating is quite pronounced. We do not see a localization of electron heating unless we observe the axis is becoming helical. These precursor oscillations can be manipulated somewhat with the ECH pulse by changing its timing and amplitude. We have very nice examples where a single gyrotron ECH pulse does not produce ∇T_e, but part way through a similar case with two gyrotrons there is an onset of $m/n=1/1$ activity accompanied by ∇T_e and an increase in $\dot{T}_e$

This is somewhat the opposite of what happens in a bean shape. In the bean shape, the successor oscillations are maximal immediately after the collapse and have disappeared by the time of the relaxation event, an interval of about 30 ms. In the first 10 or so ms, there is no clear evidence of response to an ECH pulse. In the next 10 ms, there is a peaking of T_e, but less extensive spatially than in the next 10 ms or times still later in the sawtooth cycle. This is qualitatively consistent with our description of an island structure created by the

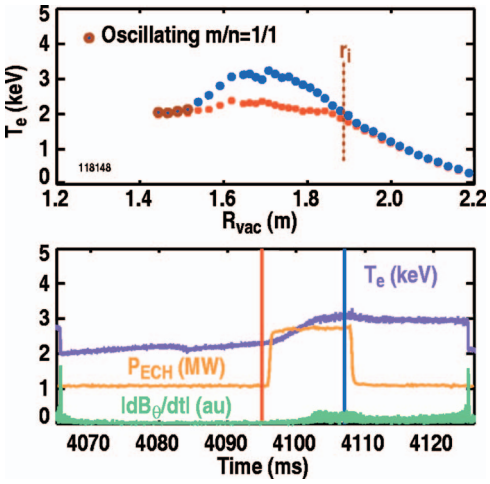

FIG. 18. (Color) (a) $T_e(R_{vac})$ (keV) for the two times indicated in (b), at the beginning and end of an ECH pulse in the oval shape. The region of $m/n=1$ activity is marked by the two-color symbol. (b) Central T_e for the single sawtooth period along with $|\dot{B}_\theta|$ at the outside midplane normalized to its peak value during the sawtooth cycle, and the ECH heating pulse displaced upward by 1 MW.

Downloaded 12 Aug 2009 to 128.83.61.90. Redistribution subject to AIP license or copyright; see http://pop.aip.org/pop/copyright.jsp

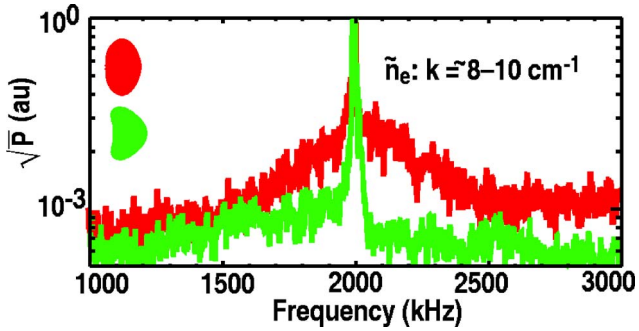

FIG. 19. (Color online) The spectrum of density fluctuations from FIR scattering for bean and oval plasmas; square root of detected power vs frequency.

collapse and vanishing before the time of the RE. In the oval, however, there is no sign of peaking prior to the onset of an $n/m=1/1$ oscillation that is dynamically visible in the ECE radial profile. This is illustrated in Fig. 18, where we have chosen, from the same discharge as in Fig. 17, a different sawtooth where the ECH pulse occurs later in the sawtooth cycle and itself excites more $m/n=1/1$ activity than would occur at that time without ECH. The phase of the 1/1 is chosen such that the flat region is seen on the inboard side. Some of the apparent radial gradient in T_e is likely to be poloidal flux compression as the axis undergoes helical motion. However, the heating rate, $\dot{T}_e$, also is increased at the onset of the 1/1 activity, providing further evidence that electron radial transport is reduced.

F. Other behaviors

We turn now to discuss the density behavior. The density is the least well measured quantity. It is obtained from the Thomson scattering with a sample every 6 ms and a large scatter compared to the statistical error, as is common with such measurements. The density profile is broad as is common in tokamaks. In the oval, we can see no regular modulation of the density. The statistical uncertainty is about 5%, whereas in the bean there is a regular variation with central density increasing about 20% through the sawtooth cycle.

Qualitatively, the sawtooth collapse in the bean shape is much more violent than it is in the oval. Overall, in the oval (case O2) there is a 16% pressure drop within the sawtooth region on the sawtooth collapse. Measurements of total stored energy do not show any modulation. In the bean there is a 42% pressure drop within the sawtooth region on the sawtooth collapse and about 15% of the total stored energy is lost from the plasma, presumably to the inner wall (the limiter).

We have also examined density fluctuations with an FIR scattering system.[24] Comparing oval and bean, a larger amplitude in density fluctuation spectra is seen in the oval (Fig. 19) at larger k and higher frequencies where $k_\theta \rho_i \sim 2-3$. This may be indicative of trapped electron modes. This would be consistent with the observation that the turbulence is seen in the electron channel while ion confinement is excellent in the oval.

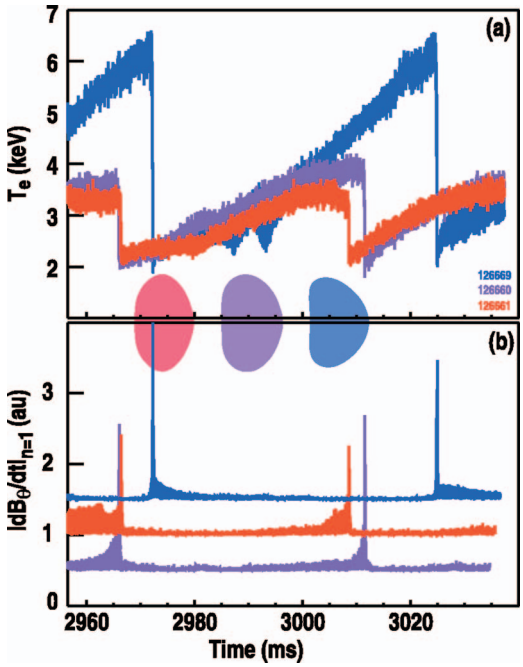

FIG. 20. (Color) (a) T_e (keV) vs time for the shapes indicated with triangularities, $\delta=0.0$, 0.20, and 0.42. (b) The $n=1$ component of $|\dot{B}_\theta|$ vs time on the same time interval. These are offset from each other for clarity. The ECH heating power is 0.7 MW in all cases.

G. Other shapes

Our comparisons of bean and oval shapes appeared so extremely different that we wondered if there might be a transition at some shape from one type of behavior to the other. To investigate this, we compared the sawtooth behavior at values of triangularity, $\delta=0.20$ and 0.42 to the oval shape. We will refer to these, $\delta=0.20$ and 0.42, as a

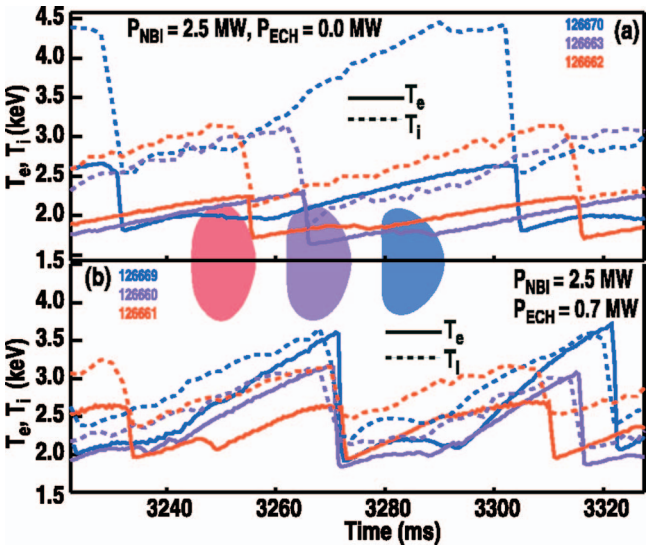

FIG. 21. (Color) (a) Electron and ion temperature response at the same spatial location, $\rho \approx 0.1$ for three shapes with only NBI. τ_S is 72, 64, and 51 ms in the moderate-D, weak-D, and oval, respectively. (b) Electron and ion temperature response at the same spatial location, $\rho \approx 0.1$, for three shapes with NBI and 0.7 MW ECH. τ_S is 51, 44, and 39 ms in the moderate-D, weak-D, and oval, respectively.

Downloaded 12 Aug 2009 to 128.83.61.90. Redistribution subject to AIP license or copyright; see http://pop.aip.org/pop/copyright.jsp

"weak-D" and "moderate-D," respectively. These results are quite new at the time of writing this paper and we can only present a cursory inspection of the data. There is some improvement in electron heating efficiency with the increase of the triangularity to $\delta=0.20$ as can be seen by an increase in electron heating efficiency with ECH. In Fig. 20(a), we show the response to ECH heating and it is improved somewhat over the oval. Here, the ECH is sustained for many sawtooth cycles, not short pulses as discussed in Sec. III E. In Fig. 20(b), we show $\dot{B}_\theta$ and note that the weak-D has precursor oscillations like the oval does and the moderate-D has successor oscillations like in the bean. Increasing to $\delta=0.42$ also had a more dramatic effect on electron heating than the increase to $\delta=0.20$.

Another view can be obtained by comparing ion and electron temperatures, as in Fig. 21(a). Here the T_e is at the position of the innermost T_i channel, 6–9 cm outside the magnetic axis. In all these shapes, the ion sawtooth amplitude is substantially larger than the electron sawtooth amplitude, whereas in a bean they are comparable. Similar data are shown in Fig. 21(b) for the case with added ECH. The sawtooth period and the ion sawtooth amplitude are always reduced when ECH is added. Also, the improvement of electron heating in the weak-D is more noticeable here than in the previous figure.

We can say that the electron heating efficiency with central ECH is better in a weak-D than in an oval and much better in a moderate-D than in an oval. The enormous increase in the ion sawtooth amplitude in the moderate-D is surprising. A valid comparison to the bean requires further study with data acquired in a single operating period. Both the ECE diagnostic and the ECH pointing antenna have been modified between the time of these data and the data shown in Fig. 10.

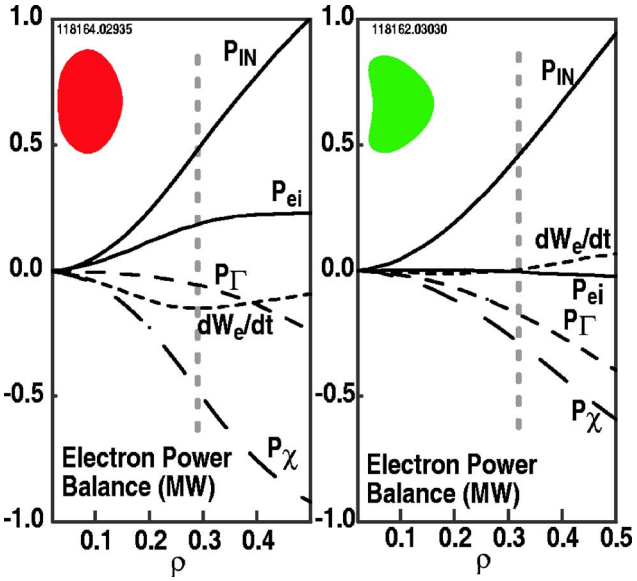

FIG. 22. (Color online) The electron power balance integrated from 0 to ρ in MW for the electrons. $P^e_{IN}, P_\chi, P_\Gamma$, and P_{ei} are the input power, and the power loss due to heat conduction, convection, and electron-ion transfer, respectively. W_e is the electron stored energy. The dashed vertical line is the $q=1$ location. $\dot{W}_e=P^e_{IN}+P_{ei}+P_\chi+P_\Gamma$.

IV. TRANSPORT AND STABILITY ANALYSIS

A. Energy transport analysis with TRANSP

We have used the TRANSP[25] code to examine electron and ion energy transport rates during the sawtooth for the discharges shown in Fig. 11, which are cases B2 and O2 of Table I. Our use of TRANSP is not quite standard and we will discuss this in some detail. Data preparation begins with reconstruction of equilibria as discussed above. These are at a 5 ms interval, averaging magnetics and MSE data over ±2 ms. Then the data for T_e, n_e, T_i, v_ϕ, and n_Z are fit as functions of toroidal flux using similar or smaller time windows. TRANSP input is then these fitted profiles along with boundary shape and q profiles from the equilibrium reconstructions, and some global data such as I_p, P_{NBI}, etc.

Initial attempts at analysis with the TRANSP code proved difficult. We found artificial effects appearing as a convective loss term. We used equilibria at 5 ms intervals and found noise did not disappear as long as the multiple equilibria were used. Conversely, if we allowed all the kinetic quantities to vary but kept a single equilibrium (boundary shape and q profile), the anomalous variation in the convective loss did not appear. TRANSP outputs a variable $\dot{\ell} \equiv \dot{\Phi}/\Phi$ as a measure of grid motion, and we saw that when the equilibrium varied $\dot{\ell}$ was of order unity, indicating unacceptably large grid motion. We also examined the terms in the Fourier expansion of R and Z from the VMEC solution inside TRANSP. For interior surfaces ($\rho<1/2$) there was no regular behavior to the high-order terms. We interpret this as follows: The number of Fourier terms required to describe the plasma boundary is much larger than 2, while at the magnetic axis only ellipticity survives and just two Fourier components are needed. We begin with 12 terms at the

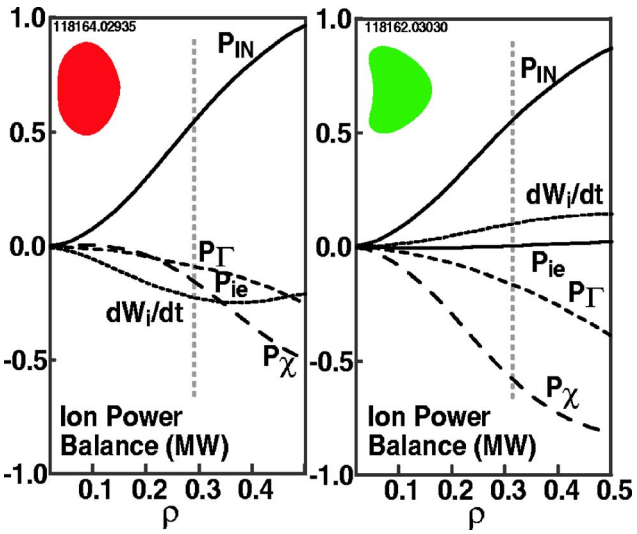

FIG. 23. (Color online) The ion power balance integrated from 0 to ρ in MW for the electrons. P^i_{IN}, P_χ, P_Γ, and P_{ie} are the input power and the power loss due to heat conduction, convection, and ion-electron transfer, respectively. W_i is the ion stored energy. The dashed vertical line is the $q=1$ location. $\dot{W}_i=P^i_{IN}+P_{ie}+P_\chi+P_\Gamma$.

Downloaded 12 Aug 2009 to 128.83.61.90. Redistribution subject to AIP license or copyright; see http://pop.aip.org/pop/copyright.jsp

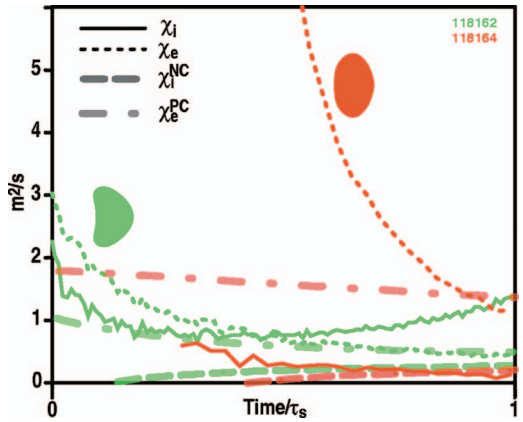

FIG. 24. (Color) The thermal diffusivities are shown for a single sawtooth period, volume-averaged from $\rho=0$ to $\rho=0.30$. χ_e and χ_i are the measured electron and ion diffusivities. χ_i^{NC} is the neoclassical ion diffusivity, and χ_e^{PC} is the paleoclassical electron diffusivity.

boundary. The six antisymmetric terms can be discarded immediately. The higher-order terms are poorly defined and serve effectively as a noise source. To remedy these problems, we decided to average the equilibria over sawteeth. Having averaged the equilibrium and thus removed the artificial convection, we felt it necessary to perform a similar average on all other quantities used as input. Our averaging procedure was to translate each input to a time base that is the sawtooth period. Then each quantity is interpolated across the time base by a regression to a function of time, either constant, linear, or quadratic. This crash-synchronized boxcar averaging worked quite well.

The integrated power balances inside the half-radius are shown in Fig. 22 for the electrons and in Fig. 23 for the ions. The loss mechanism is primarily heat conduction in both shapes. In the oval, the electron channel dominates the loss as expected from the difference in sawtooth amplitudes. In the bean shape, the ion and electron losses are comparable.

Perhaps more interesting is an odd symmetry in transport rates. The thermal diffusivities are shown volume-averaged to $\rho=0.3$ for a sawtooth cycle in Fig. 24. We also show the ion neoclassical[26] and electron paleoclassical[27] values. In the oval, the ion thermal diffusivity approximates the neoclassical value over most of the period, while the electron transport is huge. In the bean, the ion diffusivity is still low by tokamak standards, but well above neoclassical. However, in the bean the electron diffusivity is in good agreement with the paleoclassical value (itself uncertain in these conditions by a factor of 2)[28] that has been proposed as the minimum achievable value in a tokamak. In the oval the ions and in the bean the electrons are near the theoretical limits. We also note that the "rollover" in T_i in the bean during the latter part of the sawtooth cycle is associated with an increase in χ_i. It is interesting that in the oval $\chi_e \approx \chi_e^{PC}$ at the end of the sawtooth period. The reason the paleoclassical values differ between bean and oval is primarily the lower shear of the oval q profile inside r_i.

TABLE II. Fast ion loss at sawtooth collapse. Δ is the difference in value over the sawtooth collapse, U_f is the fast ion energy density, U_t is the total ion energy density, and Δt is the time from 90% to 10% of the measured Δ_N.

Case	B2	O2
Shape	Bean	Oval
Measured neutrons ($\times 10^{14}$ s^{-1})	3.65	3.40
Calculated neutrons ($\times 10^{14}$ s^{-1})	3.30	3.10
Measured Δ_N ($\times 10^{14}$ s^{-1})	−0.90	−0.30
Calculated Δ_N ($\times 10^{14}$ s^{-1})	−0.95	−0.30
$\int_{\rho=0}^{\rho=0.3} U_f dV$ (kJ)	34	36
$\Delta \int U_f dV$ (kJ)	−13	−4
$\int_{\rho=0}^{\rho=0.3} U_t dV$ (kJ)	107	128
$\Delta \int U_t dV$ (kJ)	−36	−20
Δt (μs)	~220	~360

TABLE III. Calculated growth rates for the $n=1$ mode, diamagnetic frequencies, resistive diffusion times, and normalized shear at $q=1$.

Case	B2	O2
γ_A (s^{-1})	32000	54000
ω_{*T} (s^{-1})	12000	28000
$\tau_\eta (=\mu_0 r_1^2/\eta)$ (s)	2.5	1.8
$\hat{s}_1 (=(1/q)(\partial q/\partial r))$	0.29	0.19

Fast ion transport is also affected more in the bean than the oval. From a neutron detector with 20 μs resolution, we see that the loss at the sawtooth collapse is quite fast. The drops in measured and calculated (TRANSP) neutron rates are in good agreement, indicating that the fast ion behavior is essentially correct. The comparison in Table II shows the fast ion loss at the time of collapse. The loss of fast ions from the sawtooth region is larger and faster in the bean than in the oval.

Finally, we examine the parallel electrical resistivity. In these cases, more than 80% of the plasma current inside r_i is inductive, the remainder being primarily beam-driven. We can run the same cases again with TRANSP except that we

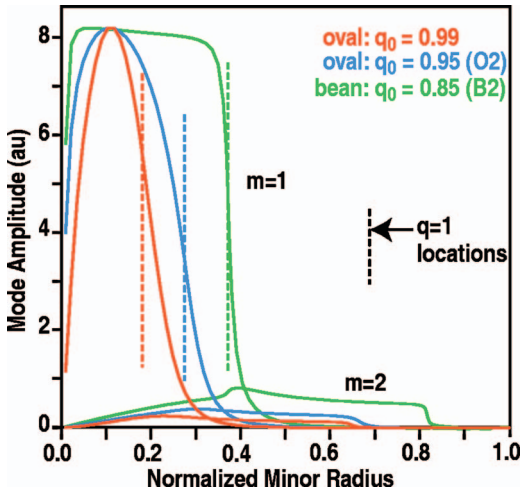

FIG. 25. (Color) $m=1$ and $m=2$ components of the $n=1$ eigenfunction. The dashed vertical lines are the location of $q=1$ in the three cases. The case with $q_0=0.99$ is like the case in Fig. 15, but with q_0 raised. Note the eigenfunction shape is quite similar to that for Fig. 15 with $q_0=0.95$.

Downloaded 12 Aug 2009 to 128.83.61.90. Redistribution subject to AIP license or copyright; see http://pop.aip.org/pop/copyright.jsp

ignore the measured q profile and instead obtain the current profile from the neoclassical calculation. Then we can compare γ_P for the two cases. In both bean and oval, we find the difference in γ_P within the interval $R=\{1.2,2.1\}$ m is less than the measurement accuracy standard deviation of 0.3 degrees. This translates to an agreement within a factor of 2.5 in resistivity between measured and neoclassical values inside the half-radius. We were seeking a difference in the plasma resistivity relative to the neoclassical value between the bean and oval shapes that might correlate with the anomalously high electron energy transport in the oval. Within experimental accuracy, no such effect was observable. The experimental uncertainty could be reduced with more data sets.

B. Stability to the $n=1$ internal mode

We have done stability analysis for cases O2 and B2 from Table I at the latest times shown in Figs. 15 and 14 using the GATO[29] code. Growth rates and diamagnetic frequencies are shown in Table III for bean and oval cases. In neither case is the diamagnetic frequency sufficiently large to play an important role. (Porcelli[30] reports that $\omega_{*i}\sim 2-4\gamma_H$ is needed.) In many ways this experiment parallels the computational work of Ref. 11, however their work focuses on stabilization at very low shear at $q=1$, $\hat{s}_1=0.04-0.07$, which are much smaller than those observed here.

For the bean, we find an instability with the eigenfunction having the "top hat" shape characteristic of the internal kink. The $m=1$ and 2 components of the eigenfunctions for cases B2 and O2 are shown in Fig. 25.

The oval case, O2, is also found to be unstable to $n=1$. (The cases O1 and B1 are also unstable.) The eigenfunction calculated by GATO is similar to that of the QI mode invoked by Wesson[4] to explain rapid sawtooth crashes on JET, although in the present case the mode is saturated and evolving slowly at the time of our analysis. Waelbroeck[31] predicted analytically the saturation of the QI mode. We have verified the interpretation of the precursor as a saturated QI mode with nonlinear MHD simulations using the NIMROD[32] code. The saturation explains the continuation of the ramp long after the ideal MHD threshold has been crossed. As expected from the single inboard phase jump in the ECE cross correlation, in the oval case the parabolic shape of the $m=1$ component of the eigenfunction shows the mode is a quasi-interchange, while the square waveform of the bean case is characteristic of an internal kink (Fig. 25).

C. Stability to interchange modes

We evaluate resistive interchange stability [the full flux surface integrals, not the axial approximation of Eq. (1)] with the BALOO[33] code, which uses the expressions from Ref. 7, thus all the geometric terms are correctly handled. Both bean and oval are unstable inside the inversion radius except for a small time interval just after collapse. Case O2 with $q_0\approx 0.95$ is shown in Fig. 26 and case B2 with $q_0\approx 0.85$ in Fig. 27. All cases we have examined show similar behavior, sustaining a pressure gradient for most of the sawtooth cycle while violating both the ideal (D_I) and resistive (D_R) inter-

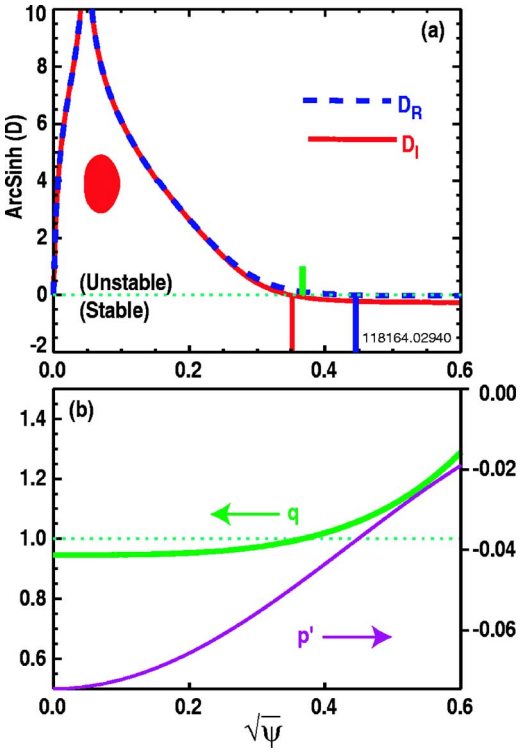

FIG. 26. (Color online) Interchange criterion; (a) the arcsinh of the interchange criterion vs $\sqrt{\psi_n}$ for both D_R and D_I and (b) q and $p'(\psi)$ vs $\sqrt{\psi_n}$. Case 02. In the upper panel the vertical bars below zero indicate the onset of instability while the vertical bar above zero is the location of $q=1$.

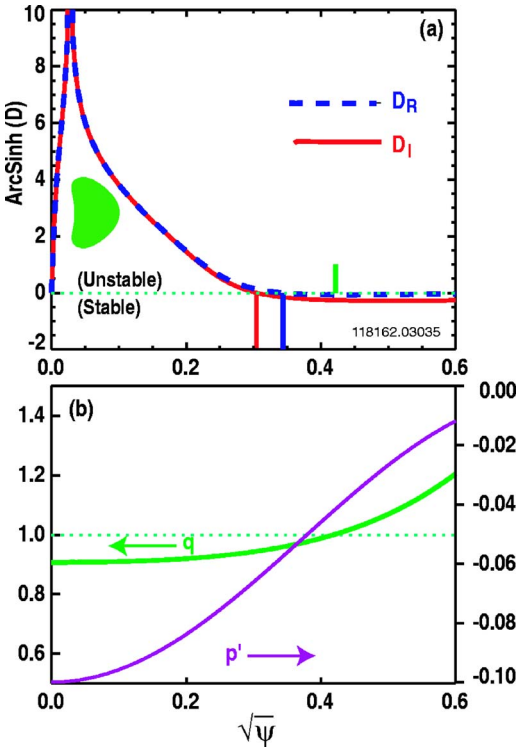

FIG. 27. (Color online) Interchange criterion; (a) the arcsinh of the interchange criterion vs $\sqrt{\psi_n}$ for both D_R and D_I and (b) q and $p'(\psi)$ vs $\sqrt{\psi_n}$. Case B2. In the upper panel, the vertical bars below zero indicate the onset of instability while the vertical bar above zero is the location of $q=1$.

Downloaded 12 Aug 2009 to 128.83.61.90. Redistribution subject to AIP license or copyright; see http://pop.aip.org/pop/copyright.jsp

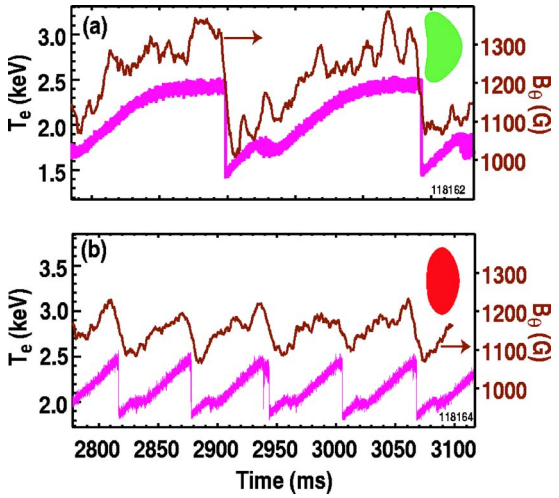

FIG. 28. (Color online) T_e and B_θ from an internal MSE channel; (a) case B2 and (b) case O2. The B_θ is boxcar-smoothed for clarity, as was discussed in Fig. 3.

change criteria over a significant fraction of the plasma minor radius. In Figs. 26 and 27 the effect of the shaping is seen in the offset of the point where $D_R=0$ from the point where $q=1$ is to the inside (lower q in the bean and to the outside to $q>1$) in the case of the oval. The plasma appears to ignore these subtle distinctions. Greene[7] shows that $D_R \sim V^{\dagger\dagger}$ and $V^{\dagger\dagger}$ can be separated into terms corresponding to magnetic well, shear $(\sim q'/q)$, and ∇p. In our cases, the latter terms are negligible and the instability occurs because the well term is positive.

The experiment began as an effort to vary the magnetic well, or average normal curvature, and observe the consequences on the sawtooth behavior. When we evaluate the normal curvature, κ_n, we find it is very near zero over the unstable region. For an axisymmetric system $\kappa_n = (1/B^2)\,\partial/\partial\psi(B^2+2\mu_0 p)$.[39] We find $\kappa_n \lesssim 0$ for both bean and oval cases. The term $(1/B^2)\,\partial/\partial\psi(B^2)$ differs substantially in the bean and oval shapes. What has happened is that p' has increased in the bean [compare Fig. 27(b) to Fig. 26(b)] so this change is canceled and both cases have similar κ_n. There is a second, smaller effect in that lower q_0 of the bean will result in a bit smaller $\langle B^2\rangle'$.

V. CONCLUDING DISCUSSION

A. The sawtooth collapse

The sawteeth in ovals and beans are qualitatively different, the former being a QI and the latter a RIK. It is commonly thought that the QI cannot occur unless q_0 is very close to unity.[1] However, calculations using GATO indicate that the eigenfunction would continue to have qualitative features of the QI with q_0 well below unity for our cases. This is shown in Fig. 25, where we have shown cases O2, B2, and O2 modified to raise q_0 but maintain the profiles.

The behavior of B_θ relative to T_e is illustrated in Fig. 28. We do see a distinct coincidence of the drop in T_e and B_θ for the bean, but we distinctly do not see such coincidence for the oval. Additionally, there is the lack of a density perturbation in the oval. The large flat regions of T_e synchronous with precursor oscillations, as shown in shown in Fig. 8, had been interpreted as islands for many years. We were surprised to find that this is not the case and these precursors are not evidence of a growing resistive internal kink mode. The preponderance of the evidence argues that the mode is a QI and there is not compelling evidence for a reconnection event on the time scale of the collapse of T_e. As we have defined the collapse time, this time is about 70 μs in the oval (Fig. 5). A common definition is the 90%–10% fall time of a central ECE channel. If we chose that definition, the time would be about 870 μs, as seen in Fig. 8(b), ignoring all the activity in Fig. 8(b), part (b1). In neither bean nor oval is tearing observed prior to the collapse. Such tearing must only occur in the last few tens of microseconds prior to collapse, or even over a similar time after collapse in the case of the bean.

In the oval during the crash, the drop in the central B_θ is slow. The nature of the crash in the oval remains unclear. The equilibrium reconstructions show that there is very little helical flux (the flux through a ribbon subtended by the axis and a $q=1$ line) in the core, and the MSE measurements indicate that the change in B_θ during the crash is likewise very small. This suggests that an electrostatic mechanism could be responsible for releasing the heat, although a magnetic reconnection process in the region where the flux is compressed by the saturation of the quasi-interchange mode may also play a role.

Recently, we have extended the range of plasma current in the oval to $I_p=1.6$ MA $(q_l \lesssim 3.5)$ thinking that the sawtooth would evolve to a resistive internal kink as q_l is lowered. The observed phenomenology is unchanged from that seen in ovals at lower plasma current. (At $I_p=1.6$ MA $\tau_S=57$ ms, $\delta T_e/T_e=0.56/1.82=0.3$, and $\delta T_i/T_i=1.26/2.17=0.6$, the n=1 precursor oscillations persist and no distinct change in γ_P is seen coincident with the collapse.)

The sawtooth collapse in the bean does not exhibit precursor oscillations. Instead, the bean has successor oscillations in which an island structure is seen. There seems little doubt of reconnection in this case as q across the central region returns to near unity from values typically 0.85. Plasma density is lost in addition to poloidal flux, furthering the generally accepted explanation of a resistive internal kink. The eigenfunction is characteristic of an internal kink. The collapse time is about 40 μs. A prompt change in the internal B_θ is seen in the MSE pitch angle for the bean but not for the oval. The magnitude of the pitch angle change for central MSE channels is substantially larger in the bean shape than in the oval, indicating a larger change in central q at the sawtooth collapse. A question to which we do not have an answer is why the sawtooth in the bean shape did not collapse much sooner. We do not believe that finite orbit effects from thermal ions should be important in the layer physics of reconnection as the ratio of poloidal gyroradius to layer width is well below unity $(\rho_i/\Delta_0 \approx 0.3)$.[34] In both shapes, the q profiles are consistent with current diffusion governed by neoclassical resistivity over a sawtooth interval.

Lastly, we note that this is the only device to report q_0 returning to unity upon sawtooth collapse. We have ex-

Downloaded 12 Aug 2009 to 128.83.61.90. Redistribution subject to AIP license or copyright; see http://pop.aip.org/pop/copyright.jsp

plained in some detail the reasons for our confidence in these results. Were these only results with strong shaping (beans), we might suspect the differences with other experiments were related to shape differences as those results were in either circular or nearly elliptical plasmas. We presently have no explanation for the difference between our results and work on other devices.

Summarizing, the change in shape results in important changes in central electron energy transport. As a result, the electron temperature is more peaked in a bean than in an oval with a somewhat higher $T_e(0)$. The resulting differences in the parallel electrical resistivity, which scales as $T_e^{3/2}$, cause the q profile to evolve differently in the two cases. This leads to a large change in central q in the bean over a sawtooth cycle, but a much smaller change with lower shear in the oval. The bean then collapses as a RIK and the oval as a QI. The difference is not demonstrated to be directly a consequence of the shape; rather, the difference is a consequence of the effect of shape on electron energy transport. The large difference in sawtooth periods between the bean and oval shapes is unexplained. The bean has been ideally unstable for most of its cycle and has shown no sign of instability until the collapse.

B. Interchange stability

We are convinced the results presented are robust, and that neither the resistive nor ideal interchange criterion is satisfied for stability over most of the central ($r < r_i$) region over most of the sawtooth period. At the same time, our attempt to change the magnetic well depth has resulted in substantial alteration in the plasma behavior. The original notion for the experiment was to make a large change in the average normal curvature, κ_n, and observe the plasma behavior. We are struck by the fact that we failed to do this in that $\kappa_n \lesssim 0$ inside r_i in both cases with no apparent limitation on ∇p. This suggests to us that there is some deficiency in the calculation of D_R; i.e., there are important physical effects missing from the calculation. We suspect the neglect of kinetic corrections[35] is the most likely deficiency. This calculation has not yet been generalized from circular to arbitrary geometry. If the modified interchange criterion were found to be satisfied, we could then conclude that the plasma response to our attempt to increase average curvature is to increase the plasma pressure, thus compensating for change in geometry by driving to a new marginal point via a change in pressure through a change in confinement. If this were not the case, we would still be faced with the fact that an attempt to vary the magnetic well results in very substantial changes in plasma properties. Energy transport and $n=1$ stability are altered, but not the magnetic well. This argues strongly that local interchange stability plays an important role in the tokamak even if we do not understand the complete theoretical treatment. Even while making this argument, we recognize that a principal finding of the experiment is the poor electron energy confinement in the oval while the ion energy confinement is excellent. This opposition seems inconsistent with processes dominated by interchange stability where one would expect the electrons to be essentially dragged along by the ions. Another example of the electrons responding differently to MHD activity than the ions is seen if we closely examine the relaxation event. The recovery is sooner in ions than electrons and this is even more dramatically true in the oval (Fig. 11) than in the bean.

These results are obtained in conditions where direct heating of electrons and ions is similar. In cases in which the majority of the power deposition is in the ions, as is common in present-day high performance experiments,[36] these effects will be less obvious. On the other hand, in an α-heated device such as ITER, they will be more severe as the ions will only be heated by energy exchange with the electrons.

C. Confinement

Electron temperature sawtooth amplitudes $\{[T_e(t_c^-) - T_e(t_c^+)]/T_e(t_c^+)\}$ and sawtooth periods are about twice as large in the bean ($\approx 2/3$) as in the oval ($\approx 1/3$). The ion temperature sawtooth amplitude ($\approx 2/3$) is much larger than the electron temperature sawtooth amplitude ($\approx 1/3$) in the oval. In the bean, the ion and electron sawtooth amplitudes are comparable. The central ion temperature stops its rise and begins to decrease at about $2/3\tau_s$. Heating with centrally deposited ECH leads to sawtooth amplitudes as large as 8/3 in a bean, while the sawtooth amplitude is little changed in the oval shape. When a short pulse ($\delta t \ll \tau_s$) of ECH is applied to a bean shape, the local heating is quite strong and strong gradients in T_e are observed to build rapidly in a manner consistent with heat diffusion as the primary transport process, as is the decay after the ECH pulse. When a short pulse of ECH is applied to the oval shape, the local heating is not observed in the absence of $m/n=1/1$ MHD activity. There is no sign of an increase in the local temperature gradient. When the axis does become helical, gradients in T_e as well as an increased heating rate are observed. The ion temperature is reduced when the electron temperature is increased with central ECH, as seen in Fig. 20. Such an inverse relationship has been seen previously.[37]

The lack of response to an ECH pulse for the oval illustrated in Fig. 17 is very stark. The lack of any visible increase in temperature gradient when the local power density increase is so large (about a factor of 25) makes it unlikely that the cause can be drift-wave turbulent transport. The fact that electron heating improves when $m/n=1/1$ activity begins suggests that the formation of a helical axis is a signature of an improvement in the quality of flux surfaces. Additionally, if we repeat our TRANSP run with $\chi_e = \sqrt{m_D/m_e}\,\chi_i$, this large χ_e is still too small to reproduce the results in the oval shape. The resulting T_e is too large as compared to the measured T_e. It is hard to imagine a radial transport for the electrons that would exceed the ion loss rate by more than the mass ratio. These results are not entirely unfamiliar. On ISX-B, in a shape similar to the oval where central electron heating was very poor, it was reported that the best electron heating occurred when the $m/n=1/1$ mode was continuous.[38]

Downloaded 12 Aug 2009 to 128.83.61.90. Redistribution subject to AIP license or copyright; see http://pop.aip.org/pop/copyright.jsp

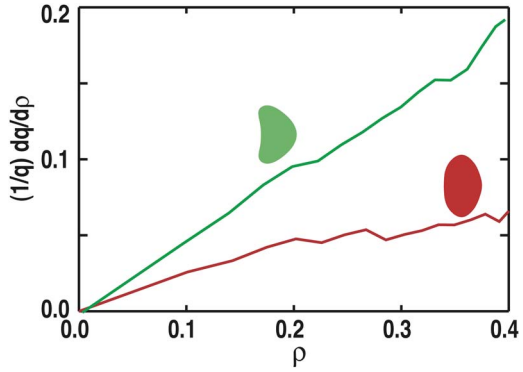

FIG. 29. (Color online) A comparison for bean and oval shapes of what central magnetic shear, $(1/q)\partial q\partial q\partial\rho$, would be *if* central J_ϕ were flat.

In the oval, the ion diffusivity is very low ($\approx$0.1 m^2/s), similar to the neoclassical value. At the scale of the ion gyroradius, the flux surfaces must be of high quality to account for the superior ion confinement while there is virtually no electron confinement. In the bean, the ion diffusivity is still at a low value ($\approx$1.0 m^2/s), about 10 times the neoclassical value.

D. Magnetic shear

We have no evidence that magnetic shear plays any significant role. There are severe changes in electron confinement with the change from bean to oval. The resulting T_e profiles lead to differences in plasma resistivity, and the differences in current profiles, and thus q, follow from the resistivity differences. However, there is also a contribution to the shear from the shaping and that differs considerably between the bean and oval shapes if J_ϕ is flat, as shown in Fig. 29. Since we see good agreement of the current profile and the neoclassical resistivity, we might assume that during the interval from the collapse to roughly the relaxation event, both T_e and J_ϕ are becoming flat. If that were so, and if the electron confinement had a significant shear dependence, it is conceivable that the bean would start with enough shear to bootstrap its way to good electron confinement while the oval had inadequate shear to do the same. Our point is not to claim that this is so, but to point out there are differences in shear when the sawtooth ramp begins that might play a role.

ACKNOWLEDGMENTS

One of us (E.A.L.) wishes to acknowledge that the origins of this experiment were conversations with J. M. Greene. We thank D. McCune for valuable assistance with TRANSP.

The work discussed in this paper was supported by the U.S. Department of Energy under Contract Nos. DE-AC05-00OR22725, DE-0FC02-04ER54698, DE-FG03-97ER54415, W-7405-ENG-48, and DE-FG02-03ER54615.

[1] R. J. Hastie, Astrophys. Space Sci. **256**, 177 (1998).
[2] S. von Goeler, W. Stodiek, and N. Sauthoff, Phys. Rev. Lett. **33**, 1201 (1974).
[3] B. B. Kadomtsev, Sov. J. Plasma Phys. **1**, 389 (1975).
[4] J. A. Wesson, Plasma Phys. Controlled Fusion **28**, 243 (1986).
[5] C. Mercier, Nucl. Fusion **1**, 47 (1960).
[6] A. H. Glasser, J. M. Greene, and J. L. Johnson, Phys. Fluids **18**, 875 (1975).
[7] J. M. Greene, Comments Plasma Phys. Controlled Fusion **17**, 389 (1997).
[8] E. A. Lazarus, F. L. Waelbroeck, T. C. Luce *et al.*, Plasma Phys. Controlled Fusion **48**, L65 (2006).
[9] B. W. Rice, D. G. Nilson, K. H. Burrell, and L. L. Lao, Rev. Sci. Instrum. **70**, 815 (1999).
[10] M. E. Austin and J. Lohr, Rev. Sci. Instrum. **74**, 1457 (2003).
[11] H. Lutjens, A. Bondeson, and G. Vlad, Nucl. Fusion **32**, 1625 (1992).
[12] K. H. Burrell, P. Gohil, R. J. Groebner, D. H. Kaplan, J. I. Robinson, and W. M. Solomon, Rev. Sci. Instrum. **75**, 3455 (2004).
[13] M.-N. Bussac, R. Pellat, D. Edry, and J. L. Soule, Phys. Rev. Lett. **35**, 1638 (1975).
[14] K. McGuire, Phys. Rev. Lett. **50**, 891 (1983).
[15] L. L. Lao, H. St. John, R. D. Stambaugh, A. G. Kellman, and W. Pfeiffer, Nucl. Fusion **25**, 1611 (1985).
[16] L. L. Lao, J. R. Ferron, R. J. Groebner *et al.*, Nucl. Fusion **30**, 1035 (1990).
[17] L. C. Appel, M. K. Bevir, and M. J. Walsh, Nucl. Fusion **41**, 169 (2001).
[18] L. L. Lao, H. E. St. John, Q. Peng *et al.*, Fusion Sci. Technol. **48**, 968 (2005).
[19] Avinash, J. B. Hastie, R. J. Taylor, and S. C. Cowley, Phys. Rev. Lett. **59**, 2647 (1987).
[20] H. Soltwisch, Rev. Sci. Instrum. **59**, 1589 (1988).
[21] J. O'Rourke, Plasma Phys. Controlled Fusion **33**, 289 (1991).
[22] F. M. Levinton, S. H. Batha, M. Yamada, and M. C. Zarnstorff, Phys. Fluids B **5**, 2554 (1993).
[23] W. W. Heidbrink, E. D. Fredrickson, T. K. Mau *et al.*, Nucl. Fusion **39**, 1369 (1999).
[24] C. L. Rettig, S. Burns, R. Philipona, W. A. Peebles, and N. C. Luhmann, Jr., Rev. Sci. Instrum. **61**, 3010 (1990).
[25] R. J. Hawryluk, in *Physics of Plasmas Close to Thermonuclear Conditions*, edited by B. Coppi *et al.* (CEC, Brussels, 1980), Vol. 1, p. 19.
[26] W. A. Houlberg, K. C. Shaing, S. P. Hirshman, and M. C. Zarnstorff, Phys. Plasmas **4**, 3230 (1997).
[27] J. D. Callen, Phys. Plasmas **12**, 092512 (2005).
[28] J. D. Callen (private communication).
[29] L. C. Bernard, F. J. Helton, and R. W. Moore, Comput. Phys. Commun. **24**, 377 (1981).
[30] F. Porcelli, Plasma Phys. Controlled Fusion **38**, 2163 (1996).
[31] F. L. Waelbroeck, Phys. Fluids B **1**, 499 (1989).
[32] A. H. Glasser, C. R. Sovinec, R. A. Nebel *et al.*, Plasma Phys. Controlled Fusion **41**, A747 (1999).
[33] R. L. Miller and J. W. VanDam, Nucl. Fusion **28**, 1201 (1987).
[34] S. Migliuolo, Nucl. Fusion **33**, 1721 (1993).
[35] F. Porcelli and M. N. Rosenbluth, Plasma Phys. Controlled Fusion **40**, 481 (1998).
[36] E. A. Lazarus, G. A. Navratil, C. M. Greenfield *et al.*, Phys. Rev. Lett. **77**, 2714 (1996).
[37] C. C. Petty, M. R. Wade, J. E. Kinsey, R. J. Groebner, T. C. Luce, and G. M. Staebler, Phys. Rev. Lett. **83**, 3661 (1999).
[38] E. A. Lazarus, J. D. Bell, C. E. Bush *et al.*, Nucl. Fusion **25**, 135 (1985).
[39] J. P. Freidberg, Rev. Mod. Phys. **54**, 801 (1982).

Downloaded 12 Aug 2009 to 128.83.61.90. Redistribution subject to AIP license or copyright; see http://pop.aip.org/pop/copyright.jsp